STRONG FIELD INTERACTIONS WITH ATOMS AND MOLECULES

SUSANA ARIAS LASO

A DISSERTATION SUBMITTED TO
THE FACULTY OF GRADUATE STUDIES
IN PARTIAL FULFILLMENT OF THE REQUIREMENTS
FOR THE DEGREE OF
DOCTOR OF PHILOSOPHY

GRADUATE PROGRAM IN PHYSICS AND ASTRONOMY
YORK UNIVERSITY
TORONTO, ONTARIO

September 4, 2020

Abstract

this is the abstract

Contents

List of Tables

List of Figures

1 Introduction

ref [3]

2 Electronic Structure of H_2O

2.1 Variational Hartree-Fock Method

2.2 Self-Consistent Field Slater Orbitals

3 H$_2$O in an external electric dc field

The dc Stark problem for the H$_2$O valence orbitals is addressed in this chapter through the implementation of a complex scaling approach that allows to study the effect of an external dc field on each molecular orbital independently. The construction of an effective potential that reflects the indivual properties of the orbitals is crucial in this analysis.

3.1 Molecular structure of H$_2$O

3.2 Partial differential equation approach to the problem

3.2.1 Exterior complex scaling

3.3 Stark resonance parameters

3.3.1 $1b_1$ and $1b_2$ molecular orbitals

3.3.2 $3a_1$ molecular orbital

4 Above threshold ionization in laser-atom and laser-molecule interactions

Generally, the interaction of an atom with intense laser fields is associated with photoionization of the atom by the absorption of one or more photons. In fact, in very intense laser fields an atom may absorb many more photons than the minimum required to get ionized, ejecting an electron of very high energy. The photoelectron energy spectrum associated with this effect exhibits a series of peaks separated by the energy of a laser photon. This phenomenon is known as above threshold ionization (ATI) and was first observed by Agostini et al [4].

ATI has been tackled by means of diverse approaches, with analytical approximations dating back to the Keldysh theory which represents a strong-field approximation [5]. Alternatively, attempts to find a numerical solution to the time-dependent Schrödinger equation (TDSE) [6–8] have been instrumental for the understanding of ATI, and a variety of efforts that deal with the complexity of solving this challenging numerical problem have been successful in the past [9]. In the same way, complementary approaches to the solution of the TDSE, such as the so-called Volkov-state methods [10–12], have revealed their strengths within strong-laser field problems in which a numerical solution would involve a computationally taxing problem. The strong-field approximation [5], which treats the binding potential of the atom as a perturbation once the electron has been promoted into the continuum where the external laser field governs the electron dynamics, is the foundation to the formalism discussed in this chapter.

Sec. 4.2 presents an overview of the pioneering work by Keldysh to describe the laser ionization of atoms. Next, a generalized approach that introduces rescattering of the electron back to the vicinity of the binding potential is included in Sec. 4.3. The ionization regime of a model He atom under a strong-laser field is explored in Sec. 4.4.1 for both scenarios: considering only direct electrons where the ionization spectrum is reproduced by the Keldysh amplitude, and

using a compact expression for the transition amplitude that encloses the limiting case of direct trajectories while allowing electrons to rescatter to the parent ion as well. Additionally, this study is extended to explore the laser ionization of the $1b_1$ and $1b_2$ molecular orbitals of H_2O in Sec. 4.4.2. The analysis presented in this chapter closely follows that of [13].

4.1 Multiphoton versus tunneling ionization

As a result of the interaction with strong laser pulses that compete with the Coulomb forces, the electron dynamics in atoms and molecules is characterized by multiphoton processes that determine their response to the laser field. The Keldysh theory of strong-field approximation illustrates how the dynamics of the underlying phenomena that contribute to the formation of ionization spectrum evolves as the laser field intensity increases [5].

At moderate intensities, $I < 10^{14}$ W/cm^2, atomic states undergo a transition from bound states into the continuum due to the multiphoton excitation linked to the interaction with the laser field, this phenomenon is known as multiphoton ionization (MPI). The interaction with intense laser fields induces an ac Stark shift of the atomic bound states that is responsible for the peak suppression in the ionization spectrum as the field intensity increases [14]. While states near the nucleus have a negligible shift in energy due their strong bond and are, in fact, harder to influence by the field, the upward shift of the higher states and continuum can become appreciable in the form of an increase in the ionization potential of the atom, I_p, see Figure 4.1(a). This shift is given by the electron ponderomotive energy, $U_p = e^2 E^2 / 4m\omega^2$, which is the cycle-averaged kinetic energy of a free electron in the electric field of strength E and frequency ω. Although this increase in the ionization potential could, possibly, make some transitions energetically forbiden, in a smoothly varying pulse ionization channels may not be closed for the entire pulse, in such a way that the corresponding peak in the ionization spectrum will not vanish completely [1, 15]. The number of photons required for MPI to take place depends on the typical binding energies of the initial states, $E_i = -I_p$. For ionization of a hydrogen atom, $I_p \sim 13.6$ eV, with a typical photon energy of $\hbar\omega \sim 1.5$ eV at 800 nm, at least 9 photons are necessary for the outer electrons to escape the binding potential of the atom and reach the continuum. While for the helium atom, $I_p \sim 24.5$ eV, under a laser photon energy of $\hbar\omega = 1.58$ eV, which we consider in this chapter, at least 15 photons are needed for ionization to occur.
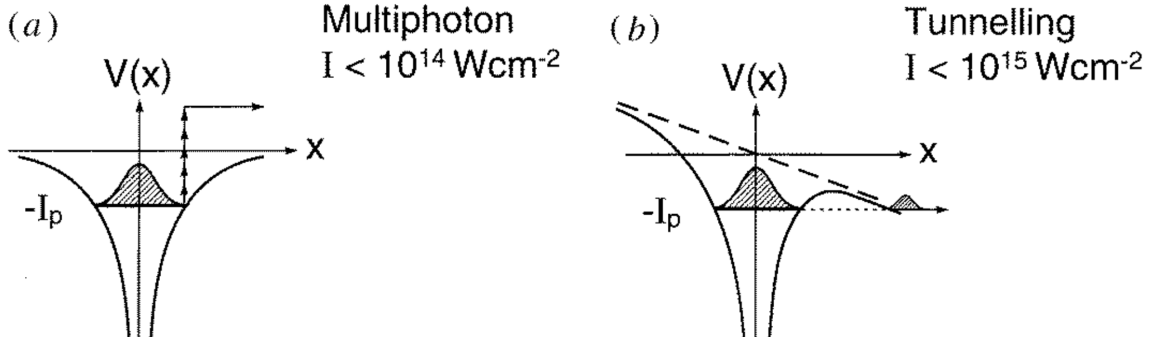
Figure 4.1: Schematic representation of (a) multiphoton ionization and (b) tunneling ionization as the laser intensity, I, increases. The dashed line corresponds to the contribution to the potential energy due to the instantaneous laser electric field. The solid line represents the full effective potential. From Ref. [1].

At sufficiently high intensity, $I > 10^{14}$ W/cm^2, and low frequency, the number of photons required for ionization grows considerably and the ionization process is ruled by a tunneling mechanism. In this regime, ionization can be described by means of a quasi-static approach in which, in the low-frequency limit, as the laser field intensity approaches the Coulomb binding potential of the ion core, the bound electrons experience an effective potential that results from the interaction between the laser electric field and the Coulomb attraction from the ion core [5]. This effective potential acts as an oscillating barrier through which electrons can escape via tunneling, as Figure 4.1(b) illustrates. In the tunneling regime, since the laser field varies slowly compared to the response time of the electron, the ionization rate becomes the cycle average of the instantaneous dc tunneling rate. A fundamental quantity in Keldysh theory, known as Keldysh parameter, is the ratio of the incident laser frequency to the tunneling rate, and can be written as [5]

$$\gamma = \frac{\omega}{\omega_t} = \sqrt{\frac{I_p}{2U_p}}, \tag{4.1}$$

where I_p is the field-free atomic ionization potential. The Keldysh parameter illustrates the limits of applicability of the competing mechanisms that characterize the ionization process. For $\gamma < 1$, tunneling dynamics will dominate, whereas for $\gamma > 1$ multiphoton dynamics will prevail. In this chapter, we will refer to the tunneling regime as it is one of the fundamental processes in ATI.
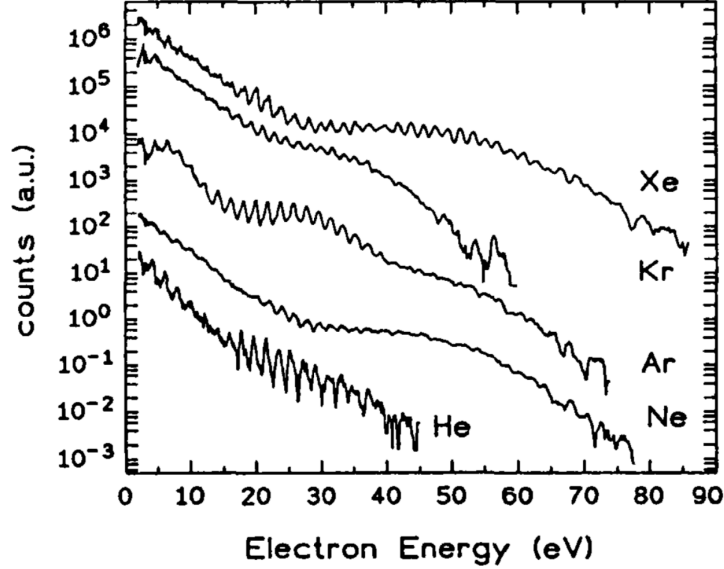
Figure 4.2: ATI spectra for various noble gases, at a wavelength of $\lambda = 630$ nm and an intensity of $I \simeq 2 \times 10^{14}$ W/cm^2 (3×10^{14} W/cm^2 for He). From Ref. [2]

4.2 Keldysh formalism

Even though the Keldysh formalism for strong-field ionization provided very good agreement with experimental data of electron ATI spectra for helium ionization [16], rescattering effects were not included in the theory and it failed to reproduce the rescattering induced plateau that is visible in measurements along a broad energy spectrum [2, 17], and emerged as a prevalent feature in the ATI energy spectrum. Figure 4.2 shows the presence of such plateau as a marked change of slope in the ionization spectrum of rare gases. A recollision picture in which the strong-field ionization is characterized by several steps, involving tunneling of the electron followed by a free interaction with the laser field in which the electron returns to the core, was introduced later on [18, 19]. In this chapter we are concerned with the numerical evaluation of an improved Keldysh approximation [13] that accounts for rescattering effects and reveals the complex structure of the ionization spectrum.

The probability amplitude for an electron to transfer from the ground state of an atom with

7

binding potential $V(\mathbf{r})$ into a scattering state $|\psi_{\mathbf{p}}(t)\rangle$ due to an external laser field is given by [13]

$$M_{\mathbf{p}} = \lim_{t\to\infty,t'\to-\infty} \langle\psi_{\mathbf{p}}(t)|U(t,t')|\psi_0(t')\rangle, \tag{4.2}$$

where it is assumed that in the limit of early times, $t' \to -\infty$, the exact wave function reduces to the unperturbed wave function $\psi_0(t)$ of the initial ground state. In order to express the total wave function in terms of the unperturbed wave function, the evolution operator formalism [20] is implemented. The time-evolution operator, $U(t,t')$, propagates the wave function $|\psi(t)\rangle$ from t' to t under the full Hamiltonian

$$H(t) = -\frac{1}{2}\nabla^2 + H_I(t) + V(\mathbf{r}), \tag{4.3}$$

which includes the binding potential of the parent ion, $V(\mathbf{r})$, and the interaction with the laser field, $H_I(t) = -\mathbf{r} \cdot \mathbf{E}(t)$, under the dipole approximation in the length gauge [13].

The time-evolution operator satisfies an integral equation, namely the Dyson equation [13, 21], which conveniently allows to construct an expansion in which the interaction with the external field is treated as a perturbation. This representation, together with the orthogonality of the initial ground state $|\psi_0\rangle$ and scattering state $|\psi_{\mathbf{p}}\rangle$, illustrates the possibility of major excursions of the scattering electron away from its parent ion once it was propagated from the initial state by $U(t,t')$.

Two approximations are crucial to derive the Keldysh result for the transition amplitude [13]. The first approximation consists of replacing the complete time-evolution operator in (4.2) by the Volkov time-evolution operator $U^V(t,t')$, which propagates the wave function of a free electron coupled through the interaction $H_I(t)$ to the external laser field. In other words, the interaction with the binding potential is considered a perturbation everywhere except in the initial and final states. In the second approximation the scattering state, $\psi_{\mathbf{p}}$, is replaced by the Volkov wave function, $\psi_{\mathbf{p}}^{(V)}$, which represents the state of a free electron in a laser field with time-averaged momentum $\mathbf{p}$. Further details about the derivation are to be found in [13]. These transformations, along with additional algebraic operations, lead to obtain an equivalent form of the standard Keldysh amplitude [13, 22]

$$M_{\mathbf{p}}^{(0)} = -i \int_{-\infty}^{\infty} dt \; \langle\psi_{\mathbf{p}}^{(V)}(t)|V|\psi_0(t)\rangle. \tag{4.4}$$

Generally, replacing the time-evolution propagator $U(t, t')$ by the Volkov propagator $U^{(V)}(t, t')$ is more justified the shorter the range of the binding potential and the higher the intensity of the laser field. In what follows, we will consider the limiting case of zero-range interactions of the form

$$V(\mathbf{r}) = -\lambda \, \delta(\mathbf{r}) \tag{4.5}$$

which has a bound state or more depending on λ [9, 23]. Zero-range potentials have been widely used in tunneling [24] and multiphoton ionization problems [25], as well as to simulate the electron dynamics in molecular systems under intense laser fields [26]. Inserting the zero-range potential (4.5) into the Keldysh amplitude (4.4) yields the expansion

$$
\begin{aligned}
M_{\mathbf{p}}^{(0)} \sim \frac{m}{2\pi} \sqrt{2m|E_0|} \sum_n \delta\left(\frac{p^2}{2m} + U_p + |E_0| - n\omega\right) \\
\times \sum_{l=-\infty}^{\infty} J_{2l+n}\left(\frac{2p_x}{\omega}\sqrt{\frac{U_p}{m}}\right) J_l\left(\frac{U_p}{2\omega}\right),
\end{aligned}
\tag{4.6}
$$

that generates the ionization spectrum of direct electrons only [13], i.e., without rescattering. After ionization, direct electrons escape the laser focus without any additional interaction with the ion. Here U_p represents the ponderomotive potential of an electron moving in the laser field with momentum $\mathbf{p}$ parallel to the laser field, $p_x = |\mathbf{p}|$, $|E_0|$ stands for the binding energy, and the J_n represent Bessel functions.

4.3 Generalized ionization amplitude including rescattering

As a result of ionization by a strong-laser field, electrons do not depart the ion vicinity immediately after tunneling the potential barrier and emerging in the continuum. Rather, they are driven by the electric field of the laser, as the field changes in sign, away and back to the core for several laser periods. Under these conditions they may scatter, at least once, off the atomic potential before finally leaving the laser pulse. Rescattering mechanisms determine the universal picture of ATI spectra [17, 23, 27], and, along with momentum conservation, represent the origin of the characteristic plateau that is present in linear-polarization generated spectra [28]. In this section, we are concerned with exploring the ATI energy spectrum of such electrons that interact further with the atomic core and rescatter.

In order to include electron rescattering in our study, it is necessary to allow the electron to interact with the parent ion once it has been freed from the binding potential. This represents a step further in relation to Keldysh theory of direct ionization [5] and it can be implemented by resorting to the Dyson expansion of the time-evolution operator in which the binding potential is considered a perturbation and the Volkov time-evolution operator plays an essential role. Inserting the expansion for the time-evolution operator into the ionization amplitude (4.2) one obtains the generalized expression [13]

$$
\begin{aligned}
M_{\mathbf{p}} = \quad & -i \lim_{t \to \infty} \int_{-\infty}^{t} dt' \langle \psi_{\mathbf{p}}(t)|U^{(V)}(t,t')\{H_I(t')|\psi_0(t')\rangle \\
& -i \int_{-\infty}^{t'} dt'' V U(t',t'')H_I(t'')|\psi_0(t'')\rangle\},
\end{aligned}
\tag{4.7}
$$

which is still an exact representation of the transition amplitude. The first term is the direct amplitude that yields the Keldysh matrix element discussed in Sec. 4.2. The second term allows for additional interactions with the atomic potential, and therefore describes rescattering of the electron. Further algebraic transformations on the second term result in the compact expression for the ionization amplitude [13]

$$
M_{\mathbf{p}} = \quad -\int_{-\infty}^{\infty} dt \int_{-\infty}^{t} dt' \langle \psi_{\mathbf{p}}^{(V)}(t)|V U^{(V)}(t,t')V|\psi_0(t')\rangle,
\tag{4.8}
$$

where the scattering state was replaced by a plane wave in order to carry out the limit of $t \to \infty$. This expression now describes both the direct electrons that depart from the atom without further interaction with the binding potential as well as the electrons that are promoted to the continuum at some time t', and propagate in the laser field until some later time t when they return to within the range of the binding potential, whereupon they rescatter into their final Volkov state.

Evaluation of the matrix element (4.8) can be very cumbersome for a finite-range binding potential. However, it simplifies noticeably in the limit of a zero-range potential of the form (4.5) where the spatial integrations become trivial. Expanding the Volkov wave function and time-evolution operator in terms of Bessel functions, one of the remaining quadratures over time can be carried out and yields the energy conserving $\delta-$function. Therefore, one quadrature is left to

10

be carried out numerically,

$$
\begin{aligned}
M_{\mathbf{P}} \sim \sum_n \delta\left(\frac{p^2}{2m} + U_p + |E_0| - n\omega\right) \sum_{l=-\infty}^{\infty} J_{2l+n}\left(\frac{2p_x}{\omega}\sqrt{\frac{U_p}{m}}\right) \\
\times \int_0^{\infty} d\tau \ \left(\frac{im}{2\pi\tau}\right)^{3/2} \left(e^{-i[|E_0|\tau + l\delta(\tau)]}\right. \\
\times \exp\left\{-iU_p\tau\left[1 - \left(\frac{\sin\frac{1}{2}\omega\tau}{\frac{1}{2}\omega\tau}\right)^2\right]\right\} \\
\left. J_l\left(y(\tau)\frac{U_p}{\omega}\right) - J_l\left(\frac{U_p}{2\omega}\right)\right),
\end{aligned}
\tag{4.9}
$$

where the real quantities $y(\tau)$ and $\delta(\tau)$ are defined via

$$
y(\tau)e^{-i\delta(\tau)} = \ \frac{1}{2} - i\left(\sin\omega\tau - \frac{4\sin^2\omega\tau/2}{\omega\tau}\right)e^{-i\omega\tau} = \ Z,
\tag{4.10}
$$

and are determined through the absolute value and phase of the complex quantity Z, respectively.

4.4 Results

4.4.1 Ionization regime. A systematic study

This section is concerned with the study of the ionization spectrum generated by a strong-laser field acting upon an atom with a binding potential that is approximated as a zero-range potential. The external laser field is assumed to be turned off in the distant past and future, $t \to \pm\infty$. With this in mind, we carry out the numerical evaluation of the transition amplitudes (4.6) and (4.9) in which we concentrate on the case of a monochromatic laser field of the form

$$
\mathbf{A} = \ A_0\hat{\mathbf{x}}\cos(\omega t).
\tag{4.11}
$$

Both contributions the one from direct electrons described by the Keldysh amplitude as well as that from rescattering electrons which interact one more time with the binding potential are considered when studying the convergence of the ATI matrix element that generates the ionization spectrum. Our calculation considers a laser field with $\hbar\omega = 1.58$ eV at an intensity of 10^{15} W/cm^2, acting upon a He atom with $E_0 = -0.9$ a.u. as the binding energy. Atomic units are used for the field intensity so the relative strengths of the laser versus the atomic binding energy are displayed.

11

The numerical evaluation of the remaining quadrature in Eq. (4.9) in terms of the travel time is not straightforward as the convergence of the solution indicates to be sensitive to the working precision requested. Given that the integrand is independent of the electron energy, associated with p_x in Eq. (4.9), a fixed value of the Bessel function order l would correspond to a single value of the integral. This allows us to explore the convergence of the individual integrals that form the sum over Bessel orders before assembling the results to be summed over the discrete energies given by n. In what follows, we will refer to the time integral as $F(l)$ by rewriting Eq. (4.9) as

$$M_{\mathbf{p}} \sim \lim_{|l|_{\max} \to \infty} \sum_n \delta\left(\frac{p^2}{2m} + U_p + |E_0| - n\omega\right) \sum_{l=-|l|_{\max}}^{|l|_{\max}} J_{2l+n}\left(\frac{2p_x}{\omega}\sqrt{\frac{U_p}{m}}\right) F(l). \qquad (4.12)$$

To study the convergence of the sum over l, we partitioned the integration interval into subintervals of $2\pi/\omega$ and explored the progression of the results as a function of how many intervals are included in the calculation as well as the working precision requested. A final interval following the $k-$th interval, $[2\pi/\omega(k-1), 2\pi/\omega k)$, that extends to $+\infty$ is included in the calculation. Additionally, in order to bypass the singularity at $\tau = 0$ due to the $1/\tau$ factor in $F(l)$, a coordinate transform of the form $x \to \sqrt{\tau}$ is implemented so that the integrand converges to a finite value as τ approaches zero. This special coordinate transform is suitable only for small values of τ given that losing the $1/\tau$ factor would slow down the convergence of the integrand to zero at larger times.

Figure 4.3 illustrates the evolution of discrete values of $F(l)$ for a set of l values, $|l| = [10, 40, 80]$, as the working precision is increased. For $l = 10$, a working precision of about 15 decimal points seems to not affect the evaluation of the integral. As l increases, the values of the integral deviate from the initial evaluation until they converge. This happens relatively quickly for negative values of l for which the graphic indicates that approximately 25 digits of precision would be enough to obtain the converged result. In contrast, for $l > 0$ the digits of precision needed increased to 50 for $l = 80$.

Given that the transition amplitude that describes the rescattering of an electron to its binding potential (4.9) is a generalization of the Keldysh amplitude (4.6) one should expect that the generalized ATI spectrum contains that of direct electrons at low electron energies. A comparison between Eqs. (4.12) and (4.6) illustrates that, for a given value of l, the function $F(l)$ should be proportional to the Bessel factor $J_l\left(\frac{U_p}{2\omega}\right)$. This calculation was carried out for
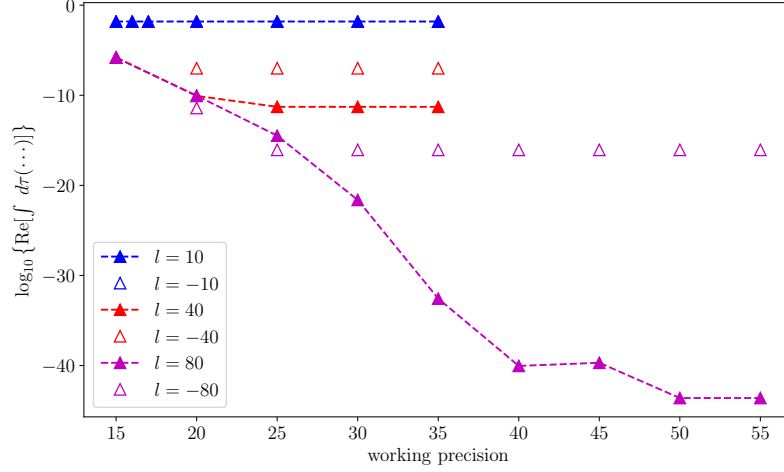
Figure 4.3: Numerical evaluation of the time integral $F(l)$ contained in the transition amplitude (4.12) for $|l| = 10, 40, 80$, indicated in blue, red and magenta respectively, as a function of the working precision requested.

different values of l in order to corroborate the validity of the aforementioned generalization.

Figure 4.4 exhibits a comparison of the numerical evaluation of $F(l)$ in (4.12) with the simple Bessel function in (4.6) for several sets of increasing values of $l_{\max}$. The coefficients that replace the integral in the Keldysh amplitude were scaled, divided by a factor of 5, so it is possible to see the agreement. For negative values of l, at about $l = -30$, the curves begin to differ as the integrals oscillate around 10^{-6} (arb. units) for a range of negative l values that extends from $l \approx -30$ to $l \approx -60$, indicating the presence of rescattering as opposed to the case for the direct transmission, shown as blue dots, from the Keldysh amplitude. As one might notice, for sufficiently small negative values of l ($l < -60$) the values of the integral start dropping below, indicating that convergence of the ionization spectrum for rescattering electrons is to be expected. As the Bessel order, l, was increased in the evaluation of the quadrature, the working precision and precision goal were tuned appropriately so the curves would remain comparable. This is consistent with Figure 4.3, as the order of Bessel functions increases, a higher working precision is required in order to find a numerical solution to the quadrature.

The ionization spectrum for the He model for emission parallel to the electric field of the
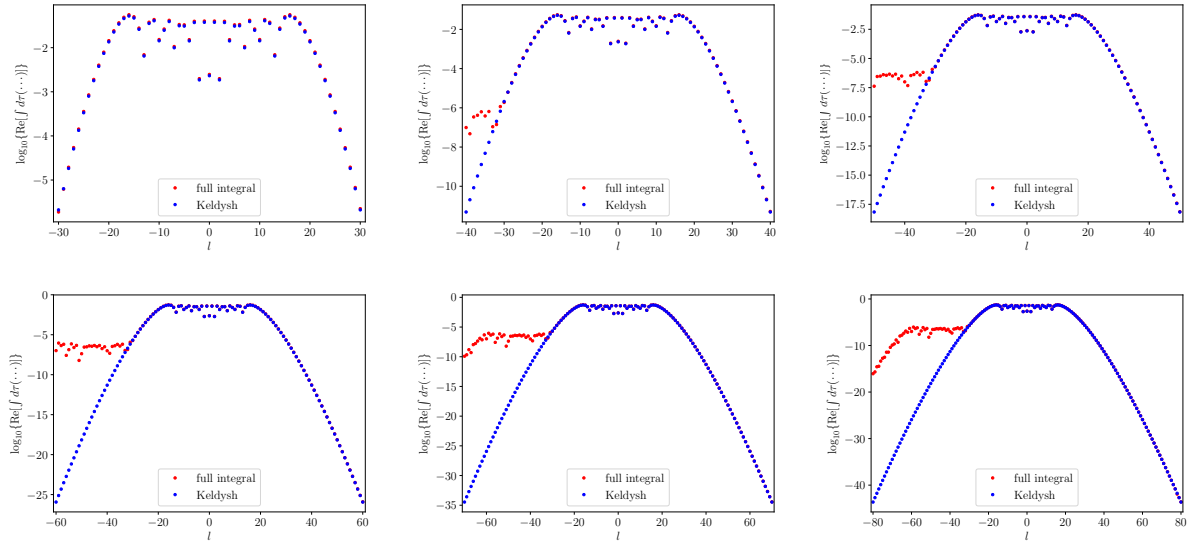
Figure 4.4: Numerical evaluation of the time integral $F(l)$ contained in the transition amplitude (4.12) (red dots) in contrast with its analogous Bessel term in the Keldysh amplitude for direct transmission (blue dots) for zero-range He atom model as a function of the Bessel function order l for increasing values of $l_{\max}$, $l = [-l_{\max}, \ldots, l_{\max}]$.
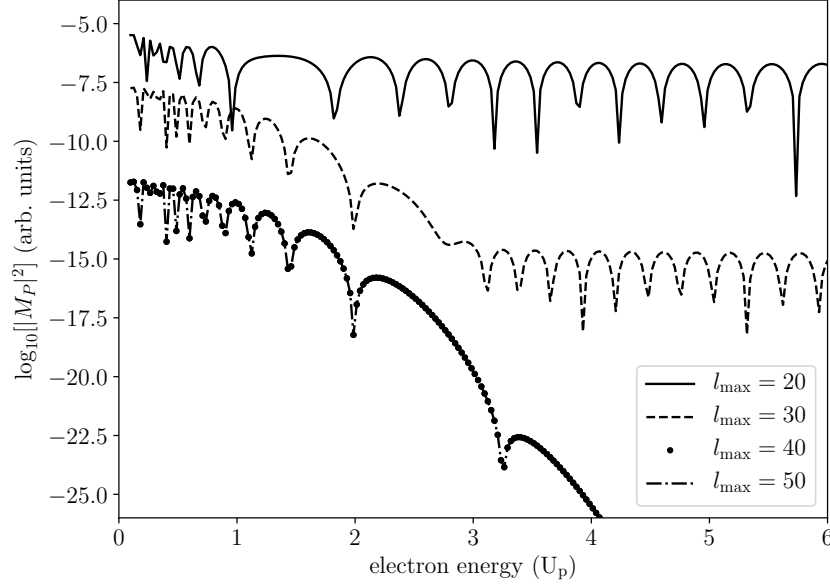
Figure 4.5: ATI spectrum of zero-range model for helium by a linearly polarized field with a laser intensity of 10^{15} W/cm^2 with $\hbar\omega = 1.58$ eV describing direct electrons. Each curve corresponds to a finite value of $l_{\max}$ in the standard Keldysh amplitude.

laser that contains the contribution of direct electrons, given by the Keldysh amplitude (4.6), is shown in Figure 4.5. For a given electron energy, the sum over the Bessel order was extended up to increasing values of $l_{\max}$, ranging from 20 to 50, in order to display the convergence of the spectrum in the limit $l \to \infty$. For $l_{\max}$ values as low as 20 and 30 the final structure of the spectrum for very small energies, $< 1U_{\mathrm{p}}$, begins to be visible. However, more terms need to be considered in the sum over Bessel functions in order to obtain the converged spectrum. The yield consisting only of direct electrons converges relatively fast to its final shape (dash-dotted line) in which a sequence of narrow suppressions of the probability amplitude separated by rounded tops drops as the electron energy increases and eventually vanishes at about 2.5U_{p}.

The results of the calculations based on (4.9) are shown in Figure 4.6. Each coloured curve represents the ionization amplitude for an atom of He under a strong-laser field for increasing values of the Bessel function order, l. As one might notice, the ionization spectrum converges for $l = 80$ (bottom right plot) after undergoing some fluctuations for l values between 40 and

70. The spectrum for direct electrons (black dots) is included as a reference. As it can be seen, both the standard Keldysh amplitude and the fully quantum mechanical result that incorporates rescattering exhibit very similar electron yields for energies lower than $2.5U_p$ where the spectrum is consisting only of direct electrons. As the electron energy increases, the rescattered electrons begin to exceed the direct ones and the curves start to differ from each other. The transition probability, consisting almost exclusively of rescattered electrons, reaches a plateau consisting of a sequence of suppressions separated by rounded tops. This behaviour is a direct consequence of quantum interference, as the released electrons interfere constructively and destructively in every optical cycle of the laser field as a function of energy. For large energies of about $10U_p$ the plateau shows a cutoff that indicates the end of the rescattering spectrum. The position of this cutoff as well as the onset energy of the plateau fluctuate with the orientation of the emitted electrons with respect to the electric field of the laser as well as with variations of the intensity of the field [2, 13, 29].

4.4.2 Ionization spectrum for the $1b_1$ and $1b_2$ orbitals of H_2O

The study on the H_2O molecular orbitals presented in Chapter 3 is extended in this section with the aim of exploring the ATI spectrum of the $1b_1$ and $1b_2$ molecular orbitals previously characterized as spherical orbitals. The zero-range model calculation carried out in the previous section combined with the strong-field approximation is applied to these valence orbitals in order to explore their response to an intense laser field.

Each molecular orbital is treated as an independent atom in which the eigenvalues ϵ_{1b_1} and ϵ_{1b_2} obtained from the radial representation of their effective potentials, $V_{\text{eff}}(r)$, are considered their binding energies, respectively. With this in mind, it is possible to generate the ionization spectrum for direct electrons and that for rescattering electrons that would correspond to each molecular orbital under a strong-laser field. Inserting the molecular binding energies into Eqs. (4.6) and (4.9) one can explore the convergence of the ionization spectrum in terms of the number of Bessel functions included in their respective sums.

Similarly to the case of strong-field ionization of a zero-range He model, the quadrature $F(l)$ in (4.12) remains to be solved in order to obtain the ionization spectrum for rescattered electrons. The general expression (4.9), which encloses the limiting case of ionization of direct

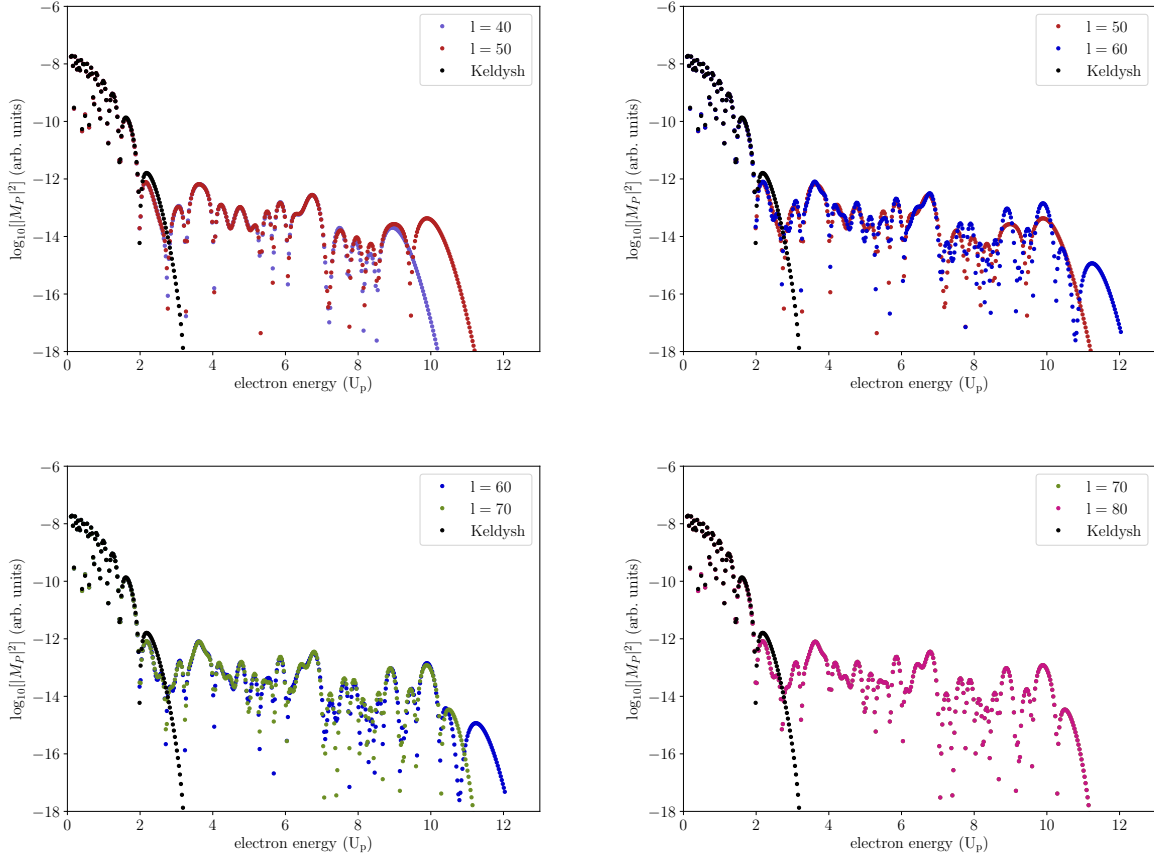Figure 4.6: ATI spectrum of a zero-range He model with a binding energy of $E_0 = -0.9$ a.u. by a linearly polarized field with a laser intensity of 10^{15} W/cm^2 with $\hbar\omega = 1.58$ eV in terms of an increasing Bessel order, l_{max}, as a function of the electron energy (in colour). The result from the standard Keldysh approximation is shown as the black dotted line.

electrons, generates an electron yield which follows that of direct electrons for low energies, i.e., electrons energies for which the direct spectrum is not vanished and the rescattering effects are not taken into account. This section is aimed to validate the previous statement and explore the convergence of the ATI spectrum of these two simplified representations of H_2O orbitals.

Figures 4.7 and 4.8 show the values taken by the function $F(l)$ for a set of values of l_{max}, $l_{max} = 30, \ldots, 80$, that indicate the extension of the sum (4.9) in terms of Bessel functions and the Bessel term in the standard Keldysh amplitude (4.6) in red and blue, respectively. The numerical values of the integral $F(l)$ were rescaled for both molecular orbitals, divided by a factor of 5.5 for the $1b_1$ MO and by a factor of 6.5 for the $1b_2$ MO, in order to make the comparability between the curves visible. Correspondingly, the working precision of the calculations was gradually increased for $|l| > 0$ up to a maximum of 50 digits of precision for $l_{max} = 80$. As it has been observed for ionization along the electric field of the laser for a He atom [13], the precise agreement between the emission rate for direct electrons and the full ionization spectrum including rescattering for energies below the cutoff of the direct-electron spectrum indicates that a correlation between the red and blue curves should be expected for a range of values of l_{max} before deviations due to rescattering become substantial. This behaviour can be observed for both molecular orbitals for $l < -30$, where the quadrature $F(l)$ reaches a plateau at about 10^{-5} that extends up to about $l < -60$ where signs of convergence of the time integral $F(l)$ become noticeable as the red curve begins to decline.

The ionization spectra corresponding to the $1b_1$ and $1b_2$ molecular orbitals are shown in Figures 4.9 and 4.10 as a function of the electron energy. The evolution of the electron yield is presented in terms of the Bessel order l, $40 \leq l \leq 80$. As it can be noticed, expanding the sum in Eq. (4.9) up to $l_{max} = 80$, purple curve, leads to convergence of the ATI spectrum for both molecular orbitals. Consistently with the comparison with the standard Keldysh amplitude shown in Figures 4.7 and 4.8, as l increases a higher working precision is needed to obtain an accurate representation of the transmission amplitude. It can be seen that the final shape of the spectrum for low energies can be obtained for l values as low as 40. For those energy values one obtains full agreement between the transmission due to direct electrons only (black curve) and the spectrum of rescattered electrons. As the electron energy increases, the Keldysh amplitudes corresponding to both orbitals $1b_1$ and $1b_2$ vanish, giving rise to the onset of the plateau that

18
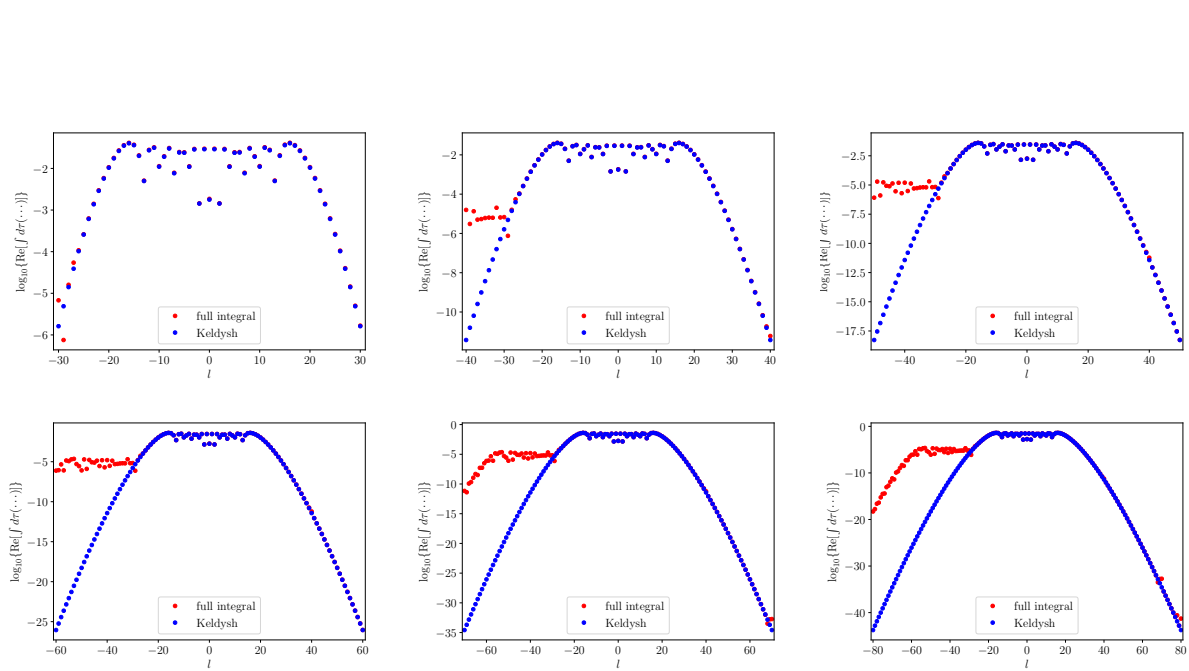
Figure 4.7: Numerical evaluation of the time integral $F(l)$ in the transition amplitude (4.12) (red dots) in contrast with its analogous Bessel term in the Keldysh amplitude for direct transmission (blue dots) for the $1b_1$ MO of H_2O as a function of the Bessel function order l for increasing values of l_{max}, $l = [-l_{max}, \ldots, l_{max}]$.
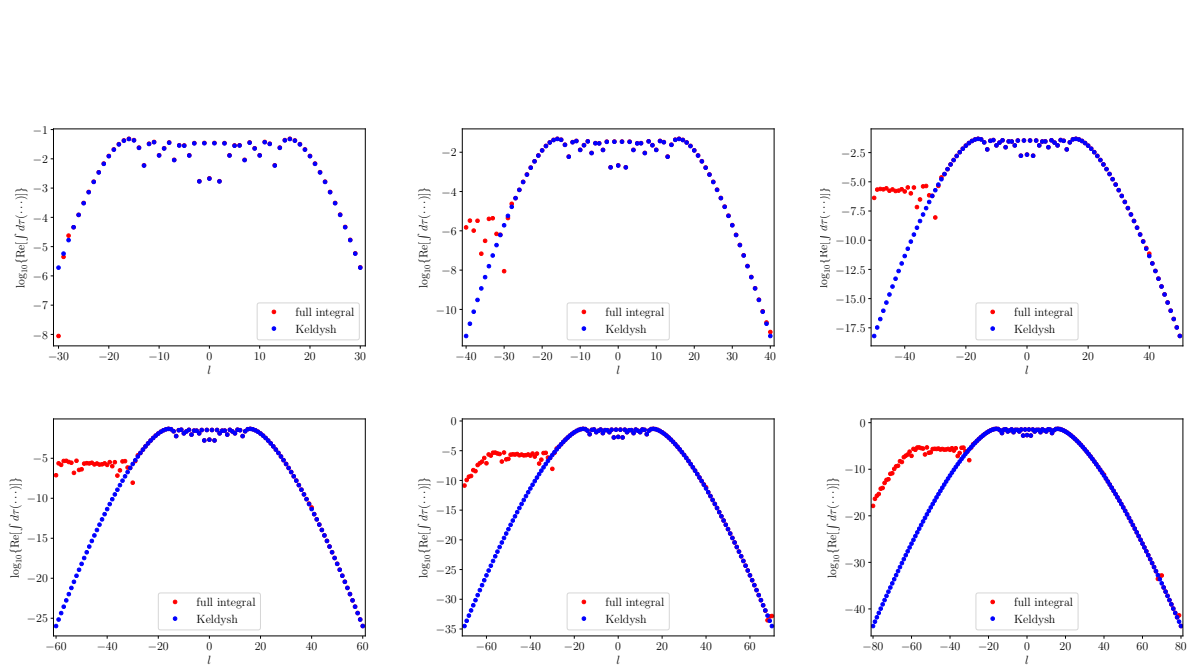
Figure 4.8: Numerical evaluation of the time integral $F(l)$ in the transition amplitude (4.12) (red dots) in contrast with its analogous Bessel term in the Keldysh amplitude for direct transmission (blue dots) for the $1b_2$ MO of H_2O as a function of the Bessel function order l for increasing values of l_{max}, $l = [-l_{max}, \ldots, l_{max}]$.
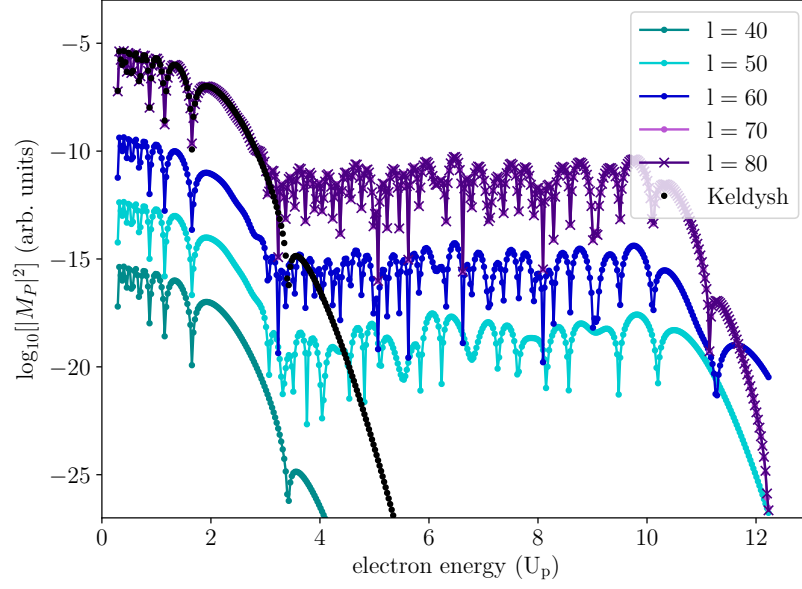
Figure 4.9: ATI spectrum for the $1b_1$ MO of H_2O by a linearly polarized field with laser intensity of 10^{15} W/cm^2 with $\hbar\omega = 1.58$ eV in terms of an increasing Bessel order, l, as a function of the electron energy (in colour). The result from the standard Keldysh approximation is shown as the black dotted line.

describes the spectrum consisting entirely of rescattered electrons.
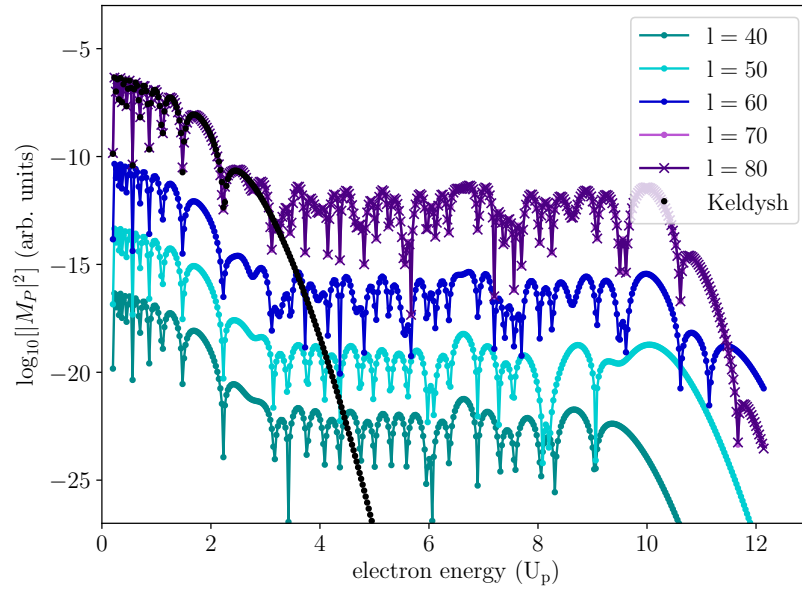
Figure 4.10: ATI spectrum for the $1b_2$ MO of H_2O by a linearly polarized field with laser intensity of 10^{15} W/cm^2 with $\hbar\omega = 1.58$ eV in terms of an increasing Bessel order, l, as a function of the electron energy (in colour). The result from the standard Keldysh approximation is shown as the black dotted line.

5 Saddle point approximation

For laser fields of sufficiently high intensity, the ATI spectrum can be generated by implementing a saddle point evaluation [19] of the multidimensional integral for the transition amplitude obtained in the previous chapter. This semi-classical approximation provides a deeper physical insight than the expansion in Bessel functions from the improved Keldysh approximation [13] as it captures the essential underlying physics. It also establishes a connection between ATI calculations within the framework of the strong-field approximation and the concept of quantum paths [30], which represent space-time trajectories of the tunneling electrons. This concept has its origins in the alternative formulation of quantum mechanics introduced by Feynman in terms of path integrals [31], where the probability amplitude of a quantum mechanical process can be represented as a coherent superposition of contributions from all possible spatio-temporal paths that connect the initial and final state of the system.

The analysis presented in this chapter establishes the connection between the quantum mechanical path integral formalism and the improved Keldysh approximation discussed in Sec. 4.3. The transition amplitude that describes the ionization of an electron under an external laser field is evaluated within the two frameworks, that in which only direct electrons are considered as well as the case that incorporates rescattering off the parent ion. Our study follows those in Refs. [13, 30].

5.1 Quantum-orbit formalism

Several quantum models have been introduced in the literature that extend the scope of Keldysh approximation for strong laser-atom interactions [13, 19, 32]. These models, which incorporate rescattering effects of the excited electrons, have been valuable in unraveling the physical phenomena behind the ATI plateau and its cutoff, an intrinsic feature of the ionization spec-

23

trum. A quasi-classical analysis of this generalization, based on the saddle point method and the path integral formalism [30, 33, 34], has been particularly useful as it elucidates fundamental aspects of the physics underlying strong-field ionization processes as well as the formation of their spectra. This approach suggests that one pictures the processes taking place in laser-atom interactions, such as ATI and high-harmonic generation (HHG), in terms of electron trajectories in phase space. These quantum trajectories follow classical Newtonian dynamics, however, must take place in the complex plane to account for tunneling ionization. Consequently, they present non-zero imaginary components which determine the probability of the process. Their physical content is reflected in the electron dynamics once it has been ionized at time t', the electron may return to its parent ion at a later time t and rescatter after propagating with momentum $\mathbf{k}$ in the continuum under the action of the external field.

In the length gauge, the compact form of the Volkov state can be expressed as [9]

$$|\psi_{\mathbf{p}}^{(V)}(t)\rangle = |\mathbf{p} - e\mathbf{A}(t)\rangle e^{-iS_{\mathbf{p}}(t)}, \tag{5.1}$$

where $|\mathbf{p} - e\mathbf{A}(t)\rangle$ represents a plane-wave state and $S_{\mathbf{p}}(t) = 1/2m \int^{t} d\tau [\mathbf{p} - e\mathbf{A}(\tau)]^2$ denotes the action of the system. Consequently, the Volkov time-evolution operator can be expressed as an expansion in terms of its Volkov states

$$U^{(V)}(t,t') = \int d^3\mathbf{k} |\psi_{\mathbf{k}}^{(V)}(t)\rangle\langle\psi_{\mathbf{k}}^{(V)}(t')|. \tag{5.2}$$

Inserting the expansion (5.2) into the matrix element (4.8) and given the time dependence of the ground state wave function, $|\psi_0(t)\rangle = \exp(iE_0 t)|\psi_0\rangle$, one may write the probability amplitude as [30]

$$M_{\mathbf{p}} = \int_{-\infty}^{\infty} dt \int_{-\infty}^{t} \int d^3\mathbf{k} \, \langle \mathbf{p} - e\mathbf{A}(t)|V|\mathbf{k} - e\mathbf{A}(t)\rangle \, \langle \mathbf{k} - e\mathbf{A}(t')|V|\psi_0\rangle$$

$$\times \exp\left[i\left(-\frac{1}{2m}\int_{t}^{\infty} d\tau[\mathbf{p} - e\mathbf{A}(\tau)]^2 - \frac{1}{2m}\int_{t'}^{t} d\tau[\mathbf{k} - e\mathbf{A}(\tau)]^2 + \int_{-\infty}^{t'} d\tau|E_0|\right)\right] \tag{5.3}$$

$$\sim \int_{-\infty}^{\infty} dt \int_{-\infty}^{t} dt' \int d^3\mathbf{k} \exp\left[iS_{\mathbf{p}}(t,t',\mathbf{k})\right] m_{\mathbf{p}}(t,t',\mathbf{k}).$$

As one may notice, the action in the exponent, $S_{\mathbf{p}}(t,t',\mathbf{k})$, contains three terms which correspond to the action of the entire system after rescattering, between ionization and rescattering, and before ionization, respectively.

It is revealing to point out the contrast of the ionization amplitude (5.3) obtained with the strong-field approximation with its analogous representation in terms of Feynman's ~~theory~~ formulation ~~of~~ path integral [31]. The time evolution operator of the entire system has the path integral representation

$$U(\mathbf{r}t, \mathbf{r}'t') = \int_{(\mathbf{r}',t') \to (\mathbf{r},t)} \mathcal{D}\left[\mathbf{r}(\tau)\right] e^{iS(t,t')}, \tag{5.4}$$

where $S(t,t') = \int_{t'}^{t} d\tau \mathcal{L}[\mathbf{r}(\tau), \tau]$ is the action calculated along a specific path by integrating the Lagrangian of the entire system along that path, and the integral measure denoted by $\mathcal{D}\left[\mathbf{r}(\tau)\right]$ establishes a coherent sum over all possible paths that connect $(\mathbf{r}t)$ and $(\mathbf{r}'t')$, independently of whether or not the paths might be followed by the actual system. This sum is, in fact, an infinite-dimensional functional of integrals, and can be reduced, within the framework of the strong-field approximation, to a sum over a few quantum orbits. By implementing the strong-field approximation we have approximated the exact action of the system at the various stages of the process: before ionization, in between ionization and rescattering, and after rescattering, as Eq. (5.3) indicates, where the ionization amplitude is computed by means of a sum over the exponential of the action over a five-parameter set of paths, parametrized by the ionization time t', the rescattering time t and the canonical momentum of the orbit in between $\mathbf{k}$ [30]. denoted by

The five-dimensional set of paths over which the transition amplitude (5.3) is evaluated can be reduced further by implementing a saddle point approximation of the integral [30], in which a handful of relevant paths remains to be considered. Since the terms of the quasi-classical action in Eq. (5.3) are proportional to I_p, U_p, p^2 and k^2, which are large under intense laser fields, the factors $\exp(-iS/\hbar)$ oscillate rapidly and the integrals in the transition amplitude can be approximated by the value of the integrands at the stationary points, saddle points, of the quasi-classical actions. The condition

$$\frac{\partial S}{\partial q_i} = 0 \tag{5.5}$$

where $q_i(i = 1, \ldots, 5)$ runs over the five variables t, t' and $\mathbf{k}$, leads to the saddle-point equa-

Some explanations are required as to what this is and why it is justified

25

tions [30, 32]

$$(\mathbf{k} - e\mathbf{A}(t'))^2 = -2m|E_0|$$
$$(\mathbf{k} - e\mathbf{A}(t))^2 = (\mathbf{p} - e\mathbf{A}(t))^2$$
$$(t - t')\mathbf{k} = \int_{t'}^{t} d\tau e\mathbf{A}(\tau). \tag{5.6}$$

The solutions $(t_S(\text{Re } t_S > \text{Re } t'_S), t'_S, \mathbf{k}_S)$, are known as the stationary points of the quasicassical action of the system, and define the quantum orbits which are the essential components in building the ionization spectrum through the saddle-point approximation. From a physical perspective, Eqs. (5.6) ensure the energy conservation at the time of tunneling, elastic scattering of the electron into its final state when it returns, and that in fact the electron returns to its parent ion, respectively. Since $|E_0| > 0$ in (5.6), the condition of energy conservation at the time of ionization cannot be satisfied for any real time t'. As a consequence, the solutions $(t_S, t'_S, \mathbf{k}_S)$ of the saddle-point equations describe complex orbits which restrains a straightforward visualization of the trajectories.

The probability amplitude (5.3) can now be expressed in terms of the saddle-point solutions as [30]

$$M_{\mathbf{p}} \sim \sum_i \left(\frac{(2\pi i \hbar)^5}{\det(\partial^2 S/\partial q_j \partial q_k)_{j,k=1,\dots,5}} \right)^{1/2} \times \exp(iS(t_{S_i}, t'_{S_i}, \mathbf{k}_{S_i})), \tag{5.7}$$

where $q_i(i = 1, \dots, 5)$ runs over the five variables t_S, t'_S and $\mathbf{k}_S$. The sum (5.7) involves a reduced set of trajectories that are sufficient to approximate the ionization spectrum through their interferences, constructive and destrutive. contributions which have

5.2 Results

This section presents the results corresponding to a saddle-point analysis of the probability amplitude to detect ATI electrons that emerge from a model-helium atom under a strong laser field of the form (4.11). In order to obtain comparable results to the quantum generalization of the strong-field approximation presented in Chapter 4, the laser intensity and frequency were set to $I = 10^{15}$ W/cm^2 and $\hbar\omega = 0.0584$ a.u., respectively.

5.2.1 Direct trajectories

The probability amplitude for detecting an ATI electron that propagates with momentum $\mathbf{p}$ in the continuum as a result of the laser irradiation of an atom, originally in its ground state, is studied in this section. The action of a system consisting of a bound electron that is ionized at time t_0, without further interaction with the parent ion, has the form [9, 36]

$$S(t_0) = -\frac{1}{2m}\int_{t_0}^{\infty} d\tau [\mathbf{p} - e\mathbf{A}(\tau)]^2 - \int_{-\infty}^{t_0} d\tau E_0, \tag{5.8}$$

where $\mathbf{A}(t)$ represents the vector potential of the laser field, and E_0 is the binding energy of the atom. As the main contribution to the transition amplitude (5.7) is given by the stationary points of the action which satisfy the condition $dS_{\mathbf{p}}/dt_0 = 0$, the integral (5.7) is evaluated by implementing a saddle-point approximation [35]. This consists in expanding the phase of the integrand, $\Phi(t) = (1/\eta)S(t) = (\omega/U_p)S(t)$, in the vicinity of the points where the phase is stationary. This results in determining the solutions of

$$\frac{\partial S}{\partial t_0} = \frac{1}{2m}(\mathbf{p} - e\mathbf{A}(t_0))^2 + |E_0| = 0. \tag{5.9}$$

The stationary points from Eq. (5.9) have a non-zero imaginary component, therefore, it is convenient to split the integral of the action (5.8) into the complex plane by implementing the substitution $\omega t_0 \to \mathrm{Re}(\omega t_0) + \mathrm{iIm}(\omega t_0)$. For a linearly polarized laser field of the form (4.11), the location of the saddle points can be determined analytically and their real and imaginary components satisfy the conditions

$$\cos^2(\mathrm{Re}\ \omega t_{0s}) = \frac{1}{2}\left(1 + \gamma^2 + \frac{E_p}{2U_p}\right) - \frac{1}{2}\sqrt{\left(\frac{E_p}{2U_p}\right)^2 + (1+\gamma^2)^2 + \frac{E_p}{U_p}(\gamma^2 - \cos 2\phi)}$$

$$\cosh(\mathrm{Im}\ \omega t_{0s}) = -\sqrt{\frac{E_p}{2U_p}}\frac{\cos\phi}{\cos(\mathrm{Re}\ \omega t_{0s})}, \tag{5.10}$$

where $m = -e = 1$, and ϕ is the angle between the momentum $\mathbf{p}$ and the direction of polarization of the laser field, $\hat{x}$. The electron energy, as it propagates in the continuum, is indicated by $E_p = p^2/2m$. As Eqs. (5.10) indicate, a single electron energy E_p is associated with four saddle-points ωt_{0s}, $s = 1, \ldots, 4$, which merge into one another by complex conjugation. These complex roots are illustrated in Figure 5.1 for electron energies within the range $(0, \ldots, 6U_p)$. The contours defined by the saddle points in phase space illustrate the integration paths to follow for a given electron energy when constructing the ATI spectrum.
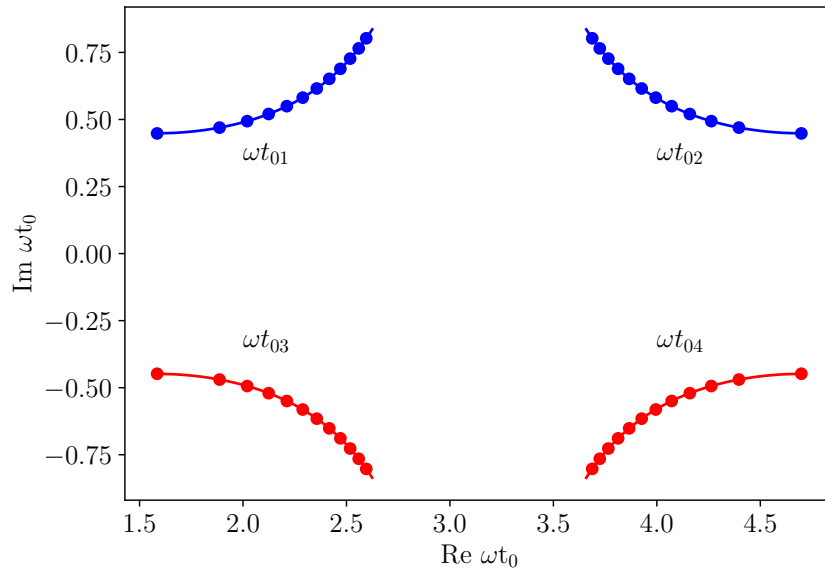
27

Figure 5.1: Saddle points obtained from Eqs. (5.10) associated with direct trajectories of electrons ionized by a linearly polarized field with laser intensity of 10^{15} W/cm^2 with $\hbar\omega = 1.58$ eV for electron energies within $E_p < 6U_p$.

This requires more explanation : the connected dots correspond to what energies?

A Taylor expansion of the action (5.8) around the saddle points allows to approximate the Keldysh-Faisal-Reiss (KFR) matrix element for direct electrons by a Gaussian function [36]

$$M_{\mathbf{p}} \sim \int_0^T dt \; e^{i\eta\Phi(t)}, \qquad (5.11)$$

where the phase is defined as $\Phi(t) = S_{\mathbf{p}}(t)\omega/U_p$, and the period of the laser field is indicated by T. The integration path to follow is defined by a contour of saddle points whose locations, given by Eq. (5.10), are known analitically for a linearly polarized laser field.

In order to visualize the regions in phase/space where the action S is stationary and, consequently, construct an integration path of stationary phase through the saddle-points, it is convenient to carry out the substitution $t \rightarrow t_r + it_i$ in Eq. (5.8). For a monochromatic laser field (4.11), and assuming that the electron path is parallel to the electric field of the laser, the real and imaginary components of the phase take the form [36]

$$\text{Im}(i\Phi(t)) = \omega t_r(1 + \frac{E_p}{U_p} + 2\gamma^2) + \frac{1}{2}\sin 2\omega t_r \cosh 2\omega t_i + 2\sqrt{\frac{2E_p}{U_p}}\sin \omega t_r \cosh \omega t_i \qquad (5.12)$$

$$-\text{Re}(i\Phi(t)) = \omega t_i(1 + \frac{E_p}{U_p} + 2\gamma^2) + \frac{1}{2}\cos 2\omega t_r \sinh 2\omega t_i + 2\sqrt{\frac{2E_p}{U_p}}\cos \omega t_r \sinh \omega t_i. \qquad (5.13)$$

At a given electron energy, the permited integration contours follow from $\text{Im}\, i\Phi(t) = \text{Im}\, i\Phi(t_{si})$, and Eq. (5.12) allows to write them explicitly as a function of $t_i(t_r)$. Figure 5.2 shows contours for constant imaginary part of the exponent in Eq. (5.11), as well as the set of saddle points corresponding to an electron energy of $2.27U_p$, indicated as $(\times)$. The blue curve corresponds to contours with $\text{Im}\, i\Phi(t) = \text{Im}\, i\Phi(t_{s_1,s_3})$, while contours with $\text{Im}\, i\Phi(t) = \text{Im}\, i\Phi(t_{s_2,s_4})$ are indicated by a red curve. The purple scale represents the real values of the exponent $i\Phi(t)$, in which dark regions indicate small values of $\text{Re}\, i\Phi(t)$, while bright regions indicate large values of $\text{Re}\, i\Phi(t)$. This indicates that, for every single electron energy, E_p, only one possible integration path is relevant in order to evaluate the transmission amplitude $M_{\mathbf{p}}$. The one starting at $t = 0$ to $+i\infty$, C_a, then along C_1 across the saddle point t_{01} up to $\omega t = \pi + i\infty$ where the integrand vanishes, from there along C_2 across the second saddle point, t_{02}, to $\omega t = 2\pi + i\infty$, and finally along C_b to $\omega t = 2\pi$. The integrands along C_a and C_b are identical and the integrals add up to zero due to the reversed integration orders. Along contours C_1 and C_2, the integrand is approximated by
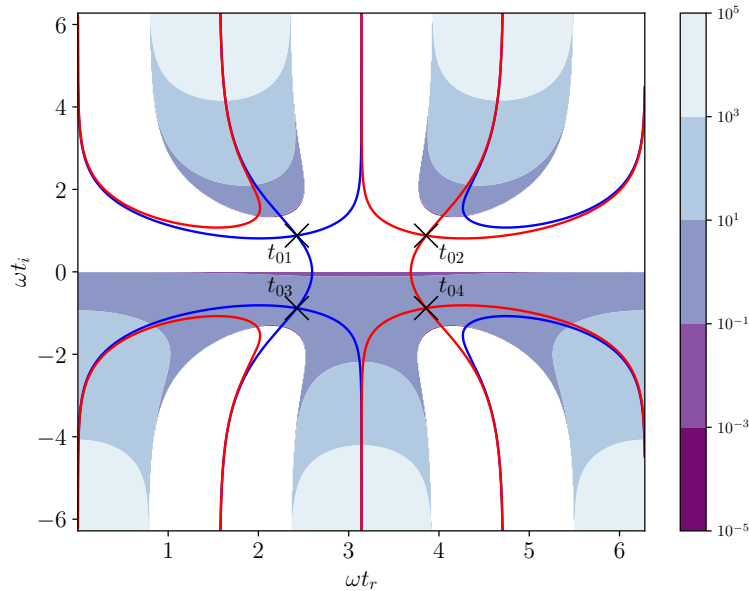
29

Figure 5.2: Phase contours of constant Im $i\Phi(t)$ for the saddle points $t_{01}(t_{03})$ (blue lines) and $t_{02}(t_{04})$ (red lines) corresponding to an electron energy of $2.27U_p$ projected on the complex plane. The regions in a purple scale represent contours of constant Re $i\Phi(t)$.

a Gaussian, which results in [36]

$$M_{\mathbf{p}} \sim \sum_{i=1,2} \sqrt{\frac{2\pi\hbar}{-iS_{\mathbf{p}}''(t_{s_i})}} \exp iS_{\mathbf{p}}(t_{s_i}). \tag{5.14}$$

Equation (5.14) approximates the ATI spectrum for an electron that, after being ionized at some time t_0 under a strong laser field, propagates within the influence of the field with no further interaction with the binding potential.

The ionization spectrum of direct electrons for a model helium atom is calculated by means of the saddle-point approximation, as Figure 5.3 displays in dash-dotted lines. Additionally, the ATI spectrum corresponding to the standard Keldysh amplitude is indicated with black dots. For a given electron energy, E_p, the probability amplitude (5.14) was evaluated along the integration trajectory that contains the saddle-points with positive imaginary parts, t_{01} and t_{02} indicated in Figure 5.1, in order to obtain a converging result when evaluating the exponential term in $M_{\mathbf{p}}$.
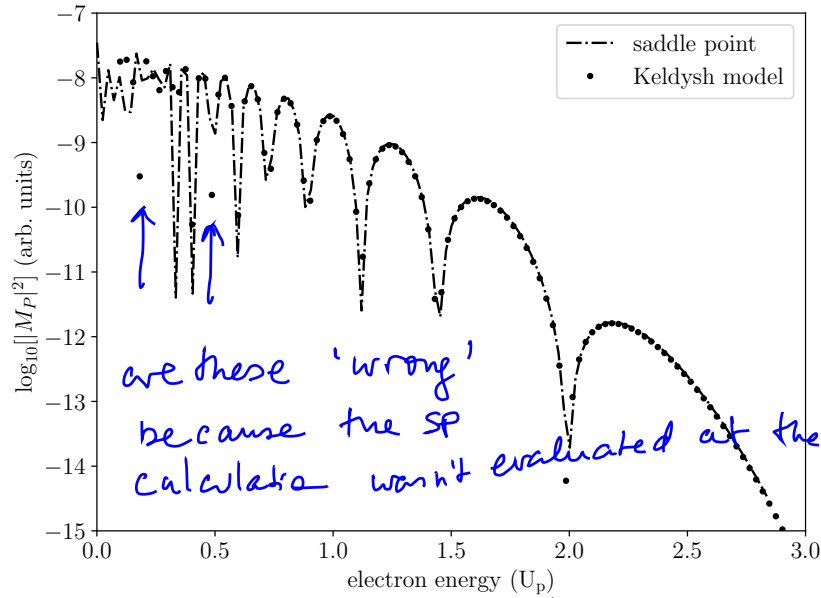
Figure 5.3: Calculated ATI spectrum using Keldysh formalism (black dots) and the saddle-point approximation (dash-dot line) in terms of trajectories 1 and 2, for a laser intensity of 10^{15} W/cm^2, $\hbar\omega = 1.58$ eV, and a binding energy of $E_0 = -0.9$ a.u. for a zero-range He model. With $\gamma = 0.654$ and $\eta = 17.9$.

The complex path of these saddle points is indicated by blue dots in Fig. 5.1 as the electron energy increases from 0 to $4U_p$. The saddle-point approximation mirrors the fully quantum calculation in terms of an expansion in Bessel functions. Similarly to what the Keldysh SFA results point out, the saddle-point approximation generates an ATI spectrum that vanishes at approximately $2.5U_p$ as the electron escapes the effects of the binding potential without further interaction with the parent ion.

5.2.2   Trajectories with rescattering

Incorporating rescattering effects in the study of ATI expands the possible physical interpretations to the ionization spectrum, in particular, it provides a comprehensible description to the origin of the ATI plateau [2, 27]. It is the purpose of this section to revisit a saddle-point approximation

of the rescattering picture in which the quantum orbits of the ionized electron play an essential part in the formation of the ATI spectrum [30].

In the recollision picture, an electron transitions from the ground state into the continuum at time t'_S, ionization time, from that time on the effects of the laser field in the electron dynamics are dominant and the Coulomb potential of the parent ion becomes negligible as the electron propagates in the continuum with momentum $\mathbf{k}_S$, however, the model accounts for further inter-action with the binding potential as the electron is considered to return to within the vicinity of the ion at time t_S, rescattering time, at which the electron acquires its final asymptotic momen-tum $\mathbf{p}$. The relevant quantum trajectories, defined by $(t'_S, t_S, \mathbf{k}_S)$, are given by the saddle-point equations (5.6) which have their origin in the condition that the action of the system remains stationary along those points. For the linearly-polarized field (4.11), after some algebraic work on the saddle-point equations, one can solve for the rescattering time and ionization time as the numerical solutions of [30]

$$[\omega t_S \mp \arccos(2\cos\omega t_S + \delta \mp i\gamma)](2\cos\omega t_S + \delta)$$
$$\pm\sqrt{1 - (2\cos\omega t_S + \delta \mp i\gamma)^2} - \sin\omega t_S = 0 \tag{5.15}$$

and

$$\omega t'_S = \mp\arccos(2\cos\omega t_S + \delta \mp i\gamma), \tag{5.16}$$

respectively, where the quantity δ is defined as $\delta = \sqrt{p^2/(4mU_p)}$. Therefore, the complex paths are generated for every possible set of $(t'_i, t_i, \mathbf{k}_i)$. As Eq. (5.15) indicates for the rescattering time, there are two possible solutions in each optical cycle $T = 2\pi$ due to the combination of signs and infinite solutions due to the multivaluedness of the arccos function. Considering the periodicity of the laser field, we can focus our attention to the interval $0 < \mathrm{Re}\, t_S < T$ for the rescattering times. Subsequently, Eq. (5.16) produces two solutions for the ionization time within the interval $-T/2 < \mathrm{Re}\, t'_S < 0$, two from the interval $-T < \mathrm{Re}\, t'_S < -T/2$, and so forth. Typically, the travel time, $\mathrm{Re}(t_S - t'_S)$, associated to a quantum trajectory indicates the relevance of its contribution to the ATI spectrum, the ones with shorter travel time being qualitatively more relevant, as they make up for the strongest contributions to the ionization spectrum.

The complex orbits for the ionization time, rescattering time and complex momentum, given by the saddle-point solutions of Eqs. (5.15) and (5.16), are shown in Figure 5.4 for trajectories

$i = (1, \ldots, 6)$ as a function of the electron kinetic energy E_p. A subset of the energy values is indicated in multiples of U_p along the paths. In the process of obtaining the saddle points corresponding to trajectories with increasing travel times, the substitution $\omega t \to \omega t + 2\pi k$, with $k = 0, 1, \ldots$, was implemented in Eqs. (5.15) and (5.16). The behaviour of these complex trajectories is markedly different depending on the location of the classical cutoff. Every pair of trajectories shows that the quantum orbits approach each other closely near the cutoff. For energies above the cutoff, the orbits in every pair diverge away from one another and the ones with negative imaginary parts stop contributing to the ATI spectrum and are dropped from the sum (5.7), as they lead to a diverging solution for the probability amplitude. This cutoff marks a turning point in the complex paths. As it can be noticed, both the rescattering times and quantum momentum have very small imaginary parts before the cutoff, while their imaginary components become noticeable as the electron energies increase beyond the cutoff. In contrast, the imaginary parts of the ionization times are significant, indicating the origin of the electrons through tunneling ionization. For energies above the cutoff, the real components of the complex paths remain approximately constant with increasing energy. As a result, a marked drop appears after the cutoff in the spectrum associated with a given pair of trajectories.

It is illustrating to take into account the complex nature of the electron dynamics in order to visualize how the action of the system, $S(t_i, t'_i, \mathbf{k}_i)$, evolves as the electron energy increases. To this end, one can write the explicit analytic expression for the action in the event that the canonical momentum $\mathbf{k}$ and the final momentum $\mathbf{p}$ are parallel to the linearly polarized laser field (4.11), which reads

$$
\begin{aligned}
S_{\mathbf{p}}(t, t', \mathbf{k}) \;=\; & -\frac{1}{2} \int_t^\infty d\tau \left[p^2 - 2eA_0 p \cos(\omega\tau) + (eA_0)^2 \cos(\omega\tau)^2 \right] \\
& -\frac{1}{2} \int_{t'}^t d\tau \left[k^2 - 2eA_0 k \cos(\omega\tau) + (eA_0)^2 \cos(\omega\tau)^2 \right] \\
& + \int_{-\infty}^{t'} d\tau |E_0|.
\end{aligned} \tag{5.17}
$$

In the vicinity of the saddle points $(t_i, t'_i, \mathbf{k}_i)$, where the action satisfies the stationarity condition (5.5), the integration limits that cause the integrand to diverge to $\pm\infty$ can be neglected. Some algebraic simplifications on the analytic expression for the action allow us to express the
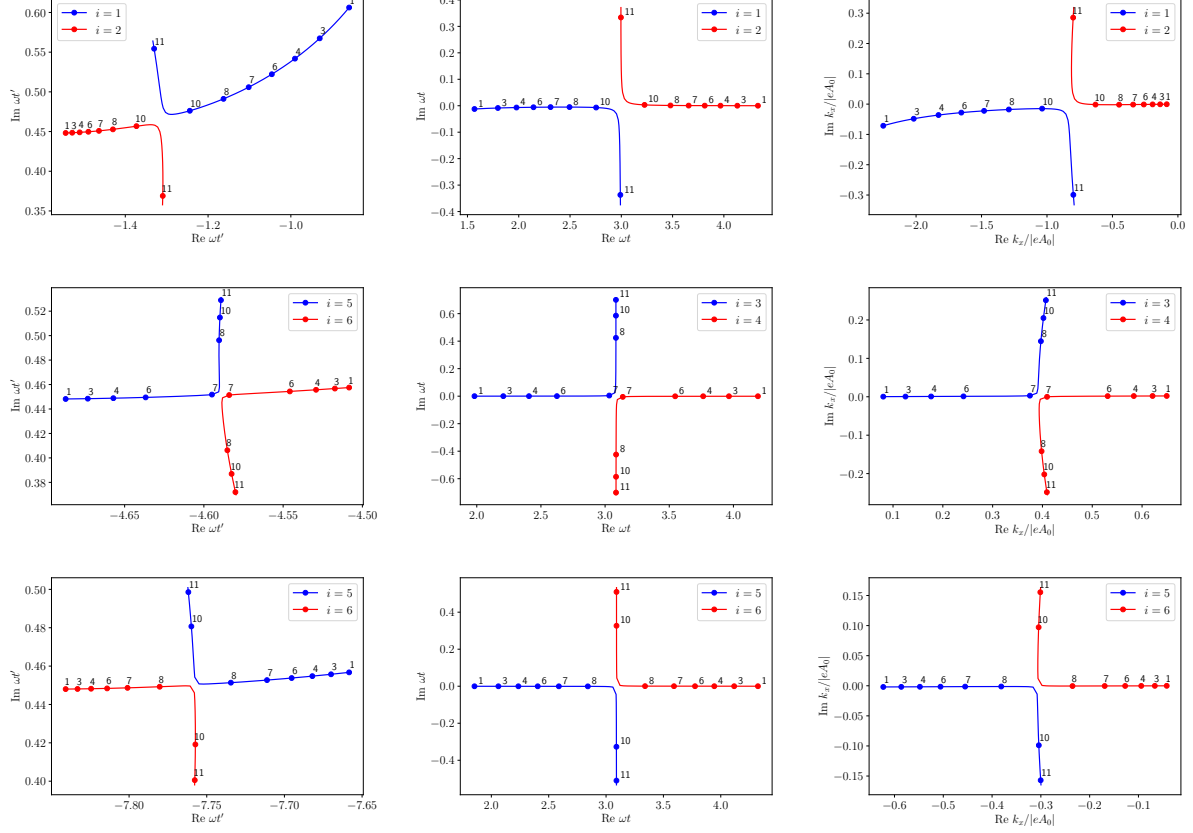
Figure 5.4: Saddle points for the orbits $(s = 1, \ldots, 6)$ in the complex plane as a function of the electron energy E_p specified along the lines in multiples of U_p. A laser field of 10^{15} W/cm^2 and $\hbar\omega = 1.58$ eV and a binding energy of $E_0 = -0.9$ a.u. were used in the calculations. In this figure, $\omega t'$ represents the ionization time, ωt stands for rescattering time, and k_x is the $x-$component of the canonical momentum $\mathbf{k}$. The underlying Keldysh parameter was set to $\gamma = 0.464$.

phase, $\Phi = (1/\eta)S$, in the probability amplitude (5.7) as

$$
\begin{aligned}
\Phi(t, t', \mathbf{k}) \;=\; & \left(\frac{E_P}{U_P} - \frac{k^2}{2U_P} \right) \omega t + \frac{2e}{\sqrt{U_P}} \left(k - \sqrt{2E_P} \right) \sin(\omega t) \\
& + \left(\frac{k^2}{2U_P} + e^2 + 2\gamma^2 \right) \omega t' - \frac{2e}{\sqrt{U_P}} k \sin(\omega t') \\
& + \frac{e^2}{2} \sin(2\omega t'),
\end{aligned}
\tag{5.18}
$$

where $E_P = p^2/2m$ indicates the electron energy.

The actions $S(t_i, t'_i, \mathbf{k}_i)/\eta$, with $\eta = 35.8$, corresponding to the electron trajectories with the shortests travel times $(i = 1, 2)$, are shown in Figure 5.5 for increasing electron energy E_p. A subset of energy values is specified along the curves up to the cutoff energy, whereupon a crossing takes place between the paths. In addition, the complex coordinates of the action extracted from [36] are included for the electron energies specified, $\times$, along with errorbars that reflect a comparison with the analytical expression for the action (5.17). For energies below the cutoff the most noticeable changes occur in the real components, while the imaginary parts of the individual trajectories change little as they approach each other along the plateau. In contrast to the saddle points behaviour (Figure 5.4), where in a given pair of trajectories (i, j) they diverge rapidly from one another towards the cutoff, the complex contributions of the action become more similar as the electron energy increases and eventually are interchanged at the cutoff, at which point one of the trajectories ceases to contribute to the ATI spectrum.

The computation of the ATI spectrum can now be carried out once the solutions of the saddle-point equations are determined. To this end, the appropriate subset of electron trajectories is inserted into the matrix element (5.7).
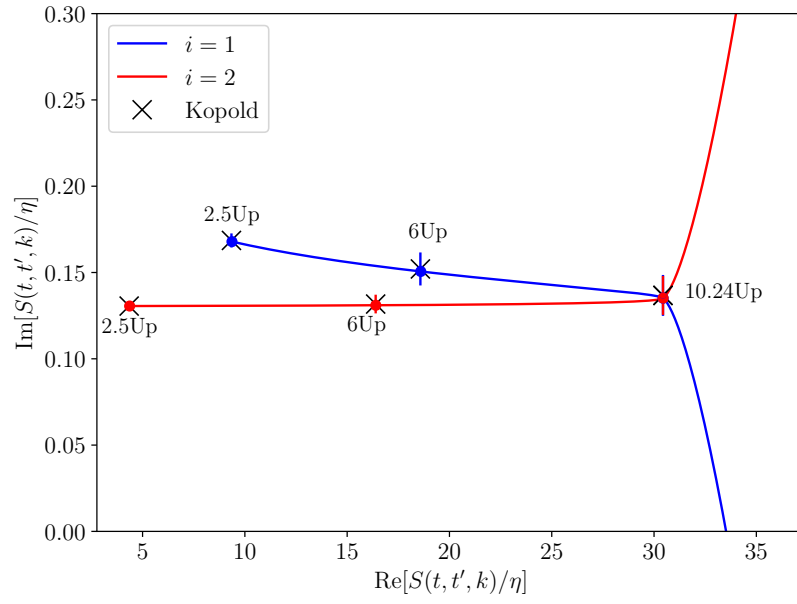
Figure 5.5: Representation of the action in the complex plane for the two shortest trajectories $(1, 2)$ shown in blue and red respectively. In addition, the complex coordinates for the action extracted from [36] are shown as $\times$ for the specified energy values.
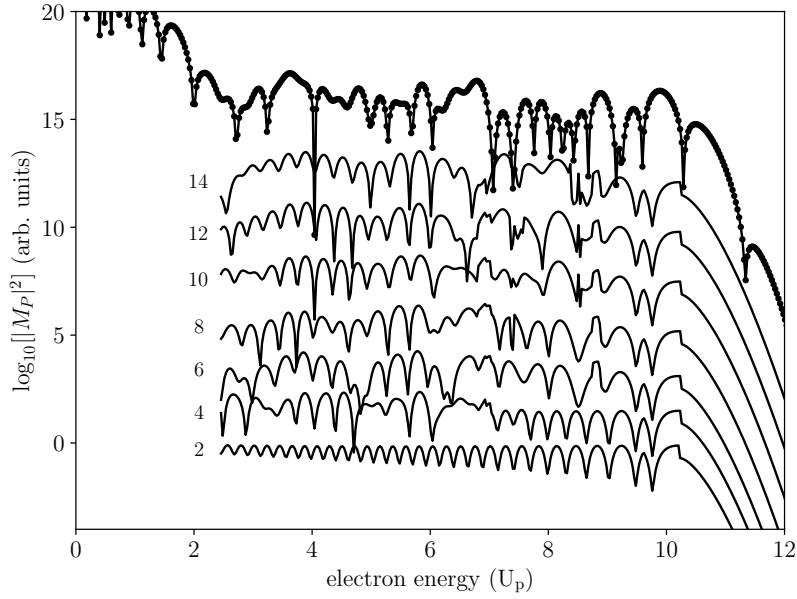
Figure 5.6: Saddle-point evaluation of the ATI spectrum as a function of the electron energy in terms of an increasing number of quantum paths. A laser intensity of 10^{15} W/cm^2 and frequency $\hbar\omega = 0.0584$ a.u. were used in the calculations, as well as a binding energy of $E_0 = -0.9$ a.u. corresponding to a model-helium atom.

6   Conclusions

Bibliography

[1] M. Protopapas, C. H Keitel, and P. L. Knight. Atomic physics with super-high intensity lasers. *Reports on Progress in Physics*, 60(4):389–486, 1997. vi, 5, 6

[2] G. G. Paulus, W. Nicklich, Huale Xu, P. Lambropoulos, and H. Walther. Plateau in above threshold ionization spectra. *Phys. Rev. Lett.*, 72:2851–2854, 1994. vi, 7, 16, 31

[3] Susana Arias Laso and Marko Horbatsch. Calculation of stark resonance parameters for valence orbitals of the water molecule. *Phys. Rev. A*, 94:053413, 2016. 1

[4] P. Agostini, F. Fabre, G. Mainfray, G. Petite, and N. K. Rahman. Free-free transitions following six-photon ionization of xenon atoms. *Phys. Rev. Lett.*, 42:1127–1130, 1979. 4

[5] L. V. Keldysh. Ionization in the field of a strong electromagnetic wave. *Soviet Physics JETP*, 20:1307–1314, 1965. 4, 5, 6, 10

[6] M. J. Nandor, M. A. Walker, L. D. Van Woerkom, and H. G. Muller. Detailed comparison of above-threshold-ionization spectra from accurate numerical integrations and high-resolution measurements. *Phys. Rev. A*, 60:R1771–R1774, 1999. 4

[7] Armin Scrinzi, Michael Geissler, and Thomas Brabec. Ionization above the coulomb barrier. *Phys. Rev. Lett.*, 83:706–709, 1999. 4

[8] C.J. Joachain, M. Dörr, and N. Kylstra. *High-Intensity Laser-Atom Physics*, volume 42 of *Advances In Atomic, Molecular, and Optical Physics*. Academic Press, 2000. 4

[9] W. Becker, F. Grasbon, R. Kopold, D.B. Milošević, G.G. Paulus, and H. Walther. *Above-Threshold Ionization: From Classical Features to Quantum Effects*, volume 48 of *Advances In Atomic, Molecular, and Optical Physics*. Academic Press, 2002. 4, 9, 24, 27

[10] F. H. M. Faisal. Collision of electrons with laser photons in a background potential. *Journal of Physics B: Atomic and Molecular Physics*, 6(11):L312–L315, 1973. 4

[11] Howard R. Reiss. Effect of an intense electromagnetic field on a weakly bound system. *Phys. Rev. A*, 22:1786–1813, 1980. 4

[12] J Z Kaminski and F Ehlotzky. Relation between sidelobes and coulomb corrections in high-order above-threshold ionization. *Journal of Physics B: Atomic, Molecular and Optical Physics*, 30(1):69–76, 1997. 4

[13] A. Lohr, M. Kleber, R. Kopold, and W. Becker. Above-threshold ionization in the tunneling regime. *Phys. Rev. A*, 55:R4003–R4006, 1997. 5, 7, 8, 9, 10, 16, 18, 23

[14] G. Petite, P. Agostini, and H. G. Muller. Intensity dependence of non-perturbative above-threshold ionisation spectra: experimental study. *Journal of Physics B: Atomic, Molecular and Optical Physics*, 21(24):4097–4105, 1988. 5

[15] C. J. Joachain, M. Dörr, and N. Kylstra. High-Intensity Laser-Atom Physics. volume 42 of *Advances In Atomic, Molecular, and Optical Physics*, pages 225 – 286. Academic Press, 2000. 5

[16] B. Walker, B. Sheehy, L. F. DiMauro, P. Agostini, K. J. Schafer, and K. C. Kulander. Precision measurement of strong field double ionization of helium. *Phys. Rev. Lett.*, 73: 1227–1230, Aug 1994. 7

[17] B. Walker, B. Sheehy, K. C. Kulander, and L. F. DiMauro. Elastic Rescattering in the Strong Field Tunneling Limit. *Phys. Rev. Lett.*, 77:5031–5034, 1996. 7, 9

[18] P. B. Corkum. Plasma perspective on strong field multiphoton ionization. *Phys. Rev. Lett.*, 71:1994–1997, 1993. 7

[19] M. Lewenstein, Ph. Balcou, M. Yu. Ivanov, Anne L'Huillier, and P. B. Corkum. Theory of high-harmonic generation by low-frequency laser fields. *Phys. Rev. A*, 49:2117–2132, 1994. 7, 23

[20] D.B. Milošević, G. G Paulus, D. Bauer, and W. Becker. Above-threshold ionization by few-cycle pulses. *Journal of Physics B: Atomic, Molecular and Optical Physics*, 39(14): R203–R262, 2006. 8

[21] Zi Jian Long and Wing-Ki Liu. Keldysh theory of strong field ionization. *Can. J. Phys.*, 88: 227–245, 2010. 8

[22] W. Becker, A. Lohr, M. Kleber, and M. Lewenstein. A unified theory of high-harmonic generation: Application to polarization properties of the harmonics. *Phys. Rev. A*, 56: 645–656, 1997. 8

[23] W Becker, A Lohr, and M Kleber. Effects of rescattering on above-threshold ionization. *Journal of Physics B: Atomic, Molecular and Optical Physics*, 27(14):L325–L332, jul 1994. 9

[24] M. Kleber. Exact solutions for time-dependent phenomena in quantum mechanics. *Physics Reports*, 236(6):331 – 393, 1994. ISSN 0370-1573. 9

[25] W. Becker, S. Long, and J. K. McIver. Short-range potential model for multiphoton detachment of the H⁻ ion. *Phys. Rev. A*, 42:4416–4419, Oct 1990. 9

[26] S. V. Borzunov, M. V. Frolov, M. Yu. Ivanov, N. L. Manakov, S. S. Marmo, and Anthony F. Starace. Zero-range-potential model for strong-field molecular processes: Dynamic polarizability and photodetachment cross section. *Phys. Rev. A*, 88:033410, 2013. 9

[27] W. Becker, S. P. Goreslavski, D. B. Milošević, and G. G. Paulus. The plateau in above-threshold ionization: the keystone of rescattering physics. *Journal of Physics B: Atomic, Molecular and Optical Physics*, 51(16):162002, 2018. 9, 31

[28] G. G. Paulus, W. Nicklich, Huale Xu, P. Lambropoulos, and H. Walther. Plateau in above threshold ionization spectra. *Phys. Rev. Lett.*, 72:2851–2854, 1994. 9

[29] G. G. Paulus, W. Becker, W. Nicklich, and H. Walther. Rescattering effects in above-threshold ionization: a classical model. *Journal of Physics B: Atomic, Molecular and Optical Physics*, 27(21):L703–L708, 1994. 16

[30] R. Kopold, W. Becker, and M. Kleber. Quantum path analysis of high-order above-threshold ionization. *Optics Communications*, 179(1):39 – 50, 2000. 23, 24, 25, 26, 32

[31] R. P. Feynman. Space-time approach to non-relativistic quantum mechanics. *Rev. Mod. Phys.*, 20:367 – 387, 1948. 23, 25

[32] M. Lewenstein, K. C. Kulander, K. J. Schafer, and P. H. Bucksbaum. Rings in above-threshold ionization: A quasiclassical analysis. *Phys. Rev. A*, 51:1495–1507, 1995. 23, 26

[33] R. Kopold, D. B. Milošević, and W. Becker. Rescattering Processes for Elliptical Polarization: A Quantum Trajectory Analysis. *Phys. Rev. Lett.*, 84:3831–3834, 2000. 24

[34] P. Salières, B. Carré, L. Le. Déroff, G. G. Paulus F. Grasbon, H. Walther, R. Kopold, W. Becker, D. B. Milosevic, A. Sanpera, and M. Lewenstein. Feynman's Path Integral Approach for Intense-Laser-Atom Interactions. *Science*, 292:902, 2001. 24

[35] A. M. Dykhne. Quantum Transitions in the Adiabatic Aproximation. *Soviet Physics JETP*, 11:411–415, 1960. 27

[36] Richard Kopold. *Atomare Ionisationsdynamik in starken Laserfeldern.* PhD thesis, Institut für Theoretische Physik, Technische Universität München, 2001. viii, 27, 29, 30, 35, 36